

MULTIFUNCTIONAL ADAPTIVE OPTICS OPTICAL COHERENCE TOMOGRAPHY ALLOWS CELLULAR SCALE REFLECTOMETRY, POLARIMETRY, AND ANGIOGRAPHY IN THE LIVING HUMAN EYE: SUPPLEMENTAL DOCUMENT

KAZUHIRO KUROKAWA* AND MORGAN NEMETH

Discoveries in Sight Research Laboratories, Devers Eye Institute, Legacy Research Institute, Legacy Health, Portland, OR 97232 USA

**kkurokawa@deverseye.org*

1. AO-OCT system design

1.1 OCT design

Figure 2 (left) shows an OCT engine based on Michelson interferometer with a polarization diversity detection channel, the main imaging system unit that captures retinal volumetric images. We designed the OCT engine to measure intrinsic optical properties, including polarization property, of retinal cells and cellular components by deploying well-established principles of single-input, single-mode-fiber (SMF) based polarization-sensitive OCT (PS-OCT) [1–4]. More specifically, we built a conventional single-input PS-OCT [5–7] but using both bulk and fiber optic for the following reasons: 1. bulk optics have robust performance, less wavelength dependency and open-air space, allowing for detailed system characterization and polarization control, and 2. combining the SMF with the paddle polarization controller (PPC) allows the flexible control of its polarization state without introducing ghost images. Since its working principle can be found elsewhere, we describe our approach from a practical perspective, including system design, implementation, and calibration process.

We utilized a polarization-maintaining (PM) fiber-coupled superluminescent diode ($\lambda=790.1 \pm 22.4$ nm, output power of 18 mW, M-S-785-B-I-15-PM, Superlum) for the OCT imaging and the AO beacon, enabling both amplitude-and phase-stable optical measurement. The linearly polarized light from the source was coupled into the slow axis of the PM fiber (PM 850, polarization crosstalk of -40 dB). Then, the light was collimated by a FiberPort (PAF2A-A10B, Thorlabs) with a $1/e^2$ beam waist diameter of 2mm. The collimated and vertically polarized light from the FiberPort was split into halves by a non-polarization cube beamsplitter (BS; BS008, Thorlabs). The reflected light entered the AO sample arm, whereas the transmitted light entered the reference arm.

In the sample illumination/detection path, the light reflected from the BS was first circularly polarized by an achromatic quarter waveplate (QWP; FBRP-AQ2, Thorlabs) with its fast axis oriented at 45° . Then, the circularly polarized light was coupled into the single mode (SM) fiber (780HP), where a PPC was placed so that the rest of the sample illumination path could mimic a polarization rotator. Therefore, the light incident on the eye was circularly polarized. The axis ratio, defined as the amplitude ratio of the major and minor axis, was 0.99 at the eye. Then, the light beam reaching the eye was focused onto the back of the eye and scanned by two high-speed galvanometric scanning mirrors (Saturn 5B 56S; ScannerMAX). The backscattered light from the sample traveled back the same illumination path in the sample arm, recoupled into the SM fiber, and re-entered into the QWP and then the BS where the returned light recombined with the reference beam.

In the reference illumination/detection path, the light first transmitted through the BS was coupled into the SM fiber (780HP) and delivered to the reference arm. The light traveled the same path length in the air as the sample arm, recoupled into the SM fiber, and then re-entered the BS where the light recombined with the sample beam. We adjusted the PPC placed on the SM fiber in the reference arm to match the spectrum shape and power between the two polarization channels by which the rest of the reference illumination/detection path can mimic

the QWP (or half waveplate (HWP) in the doubled pass) with its fast axis oriented at $22.5^\circ + 45^\circ i$ ($i = 0, 1, 2, 3$) or octadic waveplate with its fast axis oriented at $45^\circ + 90^\circ j$ ($j = 0, 1$) or any other possible combinations that equally distributed the power between the two polarization channels.

The recombined light was then split into its p- and s-polarization components by a polarization cube beamsplitter (PBS; FBT-FBS052, Thorlabs), each filtered by their respective linear polarizers (LP; LPNIR, Thorlabs), coupled into their respective SM fibers (SM-600), and delivered to their respective spectrometers (Cobra-S 800; Wasatch Photonics). The spectral interferogram was formed if the optical path length (OPL) difference of the lights returned from the reference and sample path was within the maximum depth range determined by the spectral resolution of the spectrometer. With the polarization diversity detection, the orthogonal components of the spectral interferogram were simultaneously acquired at a speed of 250 kHz with 3.29 μ s exposure by their respective high-speed frame grabbers (10 bit; 2048 pixels/line). Of note, despite the manufacturing effort in matching two spectrometers, the measured spectral interferograms were not matched well in the wavenumber domain, and thus, we corrected for residual error using Mujat et al.'s method [8]. The AO-OCT volume images were reconstructed from the spectral interferograms using a graphic processing unit (GPU) from which we computed the reflectance, retardance, optic axis orientation, and angiogram of the sample tissue (see [Section 2.2.2 Offline processing software](#) for the details).

The OCT engine was operated near the shot-noise-limited sensitivity, which was confirmed by measuring a mirror reflection with an attenuation filter. The total throughput of the OCT engine was approximately 3%, including the fiber coupling efficiency ($\sim 60\%$), the BS ($\sim 50\%$), the PBS ($\sim 50\%$), the LP ($\sim 80\%$), and the spectrometer's optics ($\sim 70\%$). To measure the sample's reflectance, we corrected the effect of signal roll-off by a simple normalization method proposed by Häusler & Lindner [9], though we used the Voigt function (a convolution of Gaussian and Lorentzian function) to model better the point spread function (PSF) of the spectrometer. Then, we derived normalized amplitude reflectance in percent by accounting for the total loss in the sample detection path. To measure the polarization property of the sample, we implemented a calibration process for the PPCs to ensure the input beam was circularly polarized. The calibration was performed before every 2-hour imaging session so that the overall polarization state of the instrument was consistent throughout all the experiments, though the calibration was not absolutely necessary to measure tissue local birefringence and local optic axis after correcting for the surface Jones matrix [10] even with SMF [11]. Typically, the axis ratio measured at the eye was reduced by 0.01% or less after 2 hours imaging session but more variable for an extended period (like a day) due to environmental factors, such as temperature change and external forces to the SMF. But other bulk optics, including QWP, were robust so that the above residual errors in the SMF were numerically canceled by measuring surface Jones matrix [11].

1.2 AO sample arm:

Figure 2 (right) shows the schematic of the AO subsystem. The AO corrects monochromatic ocular aberrations dynamically with feedback control [12,13]. For wavefront correction, we used a high-stroke deformable mirror with 97 actuators (DM; DM97 with high-stroke option; ALPAO) that can correct for most aberrations across a 7.1 mm pupil in the general population. We placed the DM closer to the eye in the AO sample arm by accounting for high refractive errors. For wavefront sensing, we used a Shack-Hartmann wavefront sensor (SHWS) built in-house with 437 lenslets to detect a tenth of the light backscattered from the eye, split by a customized dichroic mirror (DIM1 at the angle of incidence (AOI) $= 5^\circ$, R/T = 90/10 at 790 nm with polarization-independent design; T $> 90\%$ at visible light; Alluxa). The in-house SHWS consisted of an off-the-shelf lenslet array (300 μ m pitch, $f = 8.7$ mm; MALS11; Newport) and a CMOS camera (HB-1800-S-M; Emergent Vision). In front of the SHWS, we installed several optics as follows: (1) a QWP and an LP to reduce specular reflections from the optical surfaces,

(2) a band-pass filter (FF01-762/64-25; Semrock) to minimize unwanted light coming into the sensor, and (3) DIM2 (FF662-FDi01; Semrock) to reflect 95% of visible light for the fluorescence/stimulation channel and transmit 95% of the AO beacon beam for the wavefront sensing. Of note, non-common path aberrations of these optics in the SHWS arm were small and had no significant impact on the AO performance because the reference coordinates of the SHWS spots were measured using a flat mirror reflection placed after the DIM1.

Perhaps the most remarkable feature in **Fig. 2 (right)** is the four reflective off-axis afocal relay telescopes that relay the optical wavefront from the eye's pupil to DM, GMs, and SHWS. The reflective telescopes have ideal properties compared to refractive afocal telescopes (e.g., loss-less mirrors, no chromatic dispersion, and no specular reflection), but they accumulate off-axis aberrations (astigmatism and coma), causing beam wobbling (beam displacement) at the eye's pupil conjugate plane and sacrificing the dynamic range of DM for correcting the ocular aberrations. They also accumulate polarization aberrations due to the protective silver coating on the mirrors when all mirrors are aligned in the plane.

Table S1. Summary of the telescope design.

	1/e2 beam diameter [mm]	Radius of curvature [mm]	Incident angle (θ_x) [degree]	Incident angle (θ_y) [degree]
P1	7.1	Inf.	0	0
SM1		800	4	0
SM2		440	0	6
GM1*	3.9	Inf.	0	-6
SM3		440	-3	0
SM4		440	0	-3
GM2*	3.9	Inf.	0	6
SM5		440	2.65	0
SM6		1500	0	-3
DM*	13.3	Inf.	3	0
SM7		1500	-3	0
SM8		800	3	0
Eye's pupil*	7.1	Inf.	0	0

*Optical component/system that are considered as 'active'.

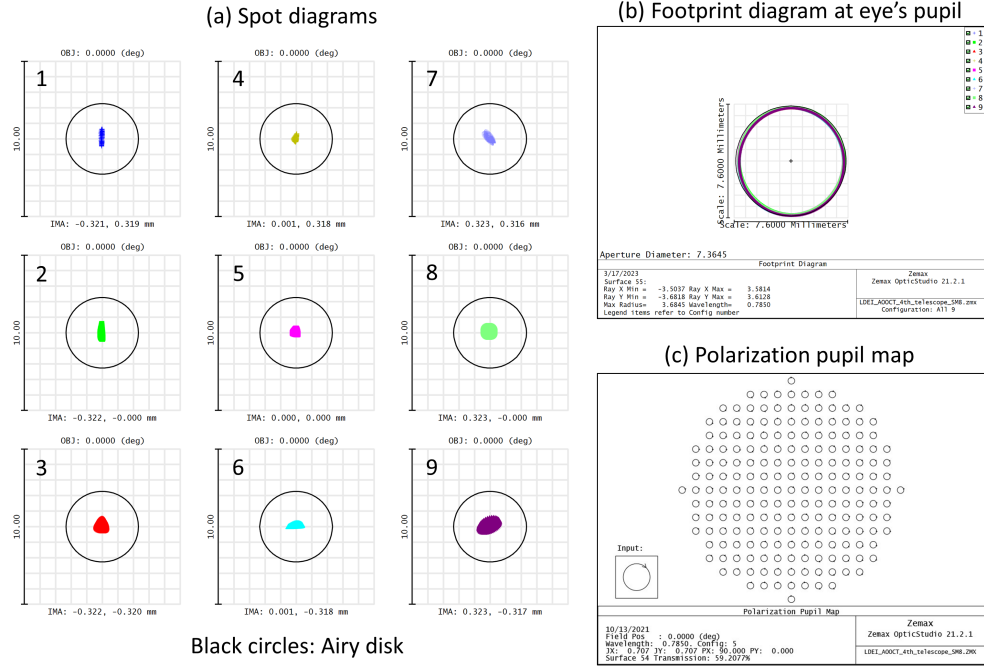


Fig. S1. Summary of Zemax simulation results: (a) spot diagrams, (b) footprint diagram at the eye's pupil, and (c) polarization pupil map. (a) The spot diagrams were obtained at 9 locations with their respective coordinates of 1. $(-1.4^\circ, 1.4^\circ)$, 2. $(-1.4^\circ, 0^\circ)$, 3. $(-1.4^\circ, -1.4^\circ)$, 4. $(0^\circ, 1.4^\circ)$, 5. $(0^\circ, 0^\circ)$, 6. $(0^\circ, -1.4^\circ)$, 7. $(1.4^\circ, 1.4^\circ)$, 8. $(1.4^\circ, 0^\circ)$, and 9. $(1.4^\circ, -1.4^\circ)$, which covers the entire field of view. All the spots were ~ 2 times smaller than the Airy disk as denoted by black circles. (b) The corresponding footprints show the minimum beam wobbling at the eye's pupil. (c) The polarization pupil map shows circularly polarized light patterns across the eye's pupil with negligible polarization aberration.

We, therefore, corrected for off-axis aberrations by deploying the straightforward approach that folds one of the spherical mirrors vertically for each telescope [14–18], which can effectively balance out polarization aberrations as well [19]. To realize this, we first prototyped the optical system using optical design software (Zemax OpticStudio). **Table S1** summarizes the details of the reflective off-axis relay telescope design comprised of 8 custom-ordered spherical mirrors with a protective silver coating (Knight Optical Inc). **Figure S1** outlines a part of Zemax simulation results, characterizing the optical performance of the designed telescopes. Our design achieved the diffraction-limited performance (Strehl ratio > 0.97) over $2.8^\circ \times 2.8^\circ$ field of view (FOV) without tilting any active optical components at the pupil conjugate plane under the constraint that the angle of incidence is less than 6° . The beam wobbling was negligible (< 0.085 mm), approximately 3.5 times smaller than each lenslet size. With protective silver coating (Material name: PROTECTIVE_SILVER) on all the mirror surfaces in Zemax, the diattenuation was 0.002, ten times less or smaller than corneal diattenuation (~ 0.03 reported in the bovine cornea [20]), negligible in PS-OCT measurements [10,21,22]. With the optical design, we carefully chose the optomechanical component for each optic with 3D CAD software (Autodesk Fusion 360) and aligned the optics accordingly.

After the construction, we measured (1) beam wobbling, (2) DM actuation required for the system aberration correction, and (3) the linear diattenuation in the AO sample arm. The wobbling was measured by scanning the beam over 2.5° FOV and measuring the beam position via a no-lens camera. We found the maximum beam displacement of 0.1 mm, three times

smaller than each lenslet size. Next, we measured the system aberration with a model eye consisting of highly scattering media (heavy white paper) and an achromatic lens with a focal length of 30 mm. The dominant aberration, including the lens aberration, was a 3rd-order spherical aberration ($c_4^0=0.086\text{ }\mu\text{m}$) followed by astigmatism ($c_2^{-2}=0.064\text{ }\mu\text{m}$ and $c_2^2=-0.060\text{ }\mu\text{m}$), including the lens aberration, totaling an RMS wavefront error of $0.16\text{ }\mu\text{m}$. However, the most severe aberration was from the DM itself; the RMS wavefront error jumped up to 18 times immediately after the DM was powered on and set to flat (zero voltages), which could be reduced by adjusting the sample position (defocus). Still, the RMS error was four times worse than without powering the DM. Nonetheless, such aberrations were corrected after closing the AO loop, which required only 7% DM stroke at maximum. In other words, the rest of the 93% DM stroke was available for ocular aberration correction. Finally, the linear diattenuation was estimated by measuring power throughput after placing and rotating an additional LP immediately after the collimator. The measured diattenuation, including the diattenuation of DIM1 (0.001), was 0.01, less than that of corneal diattenuation (0.03). The residual retardance remaining in the AO sample arm was canceled by the calibration process in which the input beam was circularly polarized (see Subsection S1.1).

1.3 Fluorescence/stimulation channel:

Another important aspect of the AO-OCT system design includes an additional fluorescence/stimulation channel (see Fig. 1) that enables simultaneous AO-OCT and AO fluorescence imaging and configurable visual stimulation. Since their working principles are well documented elsewhere for each [23–26], we choose to describe the system design and hardware implementation specific to our device. Further details for each channel will be given for their specific use-case scenarios in separate on-going studies.

We enabled the simultaneous imaging/stimulation with AO by splitting the 800-nm wavelength band AO-OCT beam from the visible light using DIM2 (FF662-FDi01; Semrock), which reflects 95% of visible light for the fluorescence/stimulation channel. The visual stimulation channel had an LED-based DLP projector (DLP® E4500MKII, EKB Technology Ltd.), generating bright and high contrast color images with a rapid on/off switching capability for making diverse spatial and temporal illumination patterns across wavelengths to stimulate different types of retinal cells and components [25,26]. The fluorescence channel was implemented, but specifically for non-human primate (NHP) imaging, providing the detection of autofluorescence and the most common experimental fluorophores, such as fluorescein isothiocyanate (FITC) and green fluorescent protein (GFP). We used an off-the-shelf dichroic mirror combined with notch filters (MDF-GFP2, Thorlabs) that reflect the excitation beam ($482 \pm 9\text{ nm}$ wavelength light) and transmit the emission beam ($520 \pm 14\text{ nm}$ wavelength light), but also leave flexibility for selecting the wavelengths in order to detect other families of fluorophore for future studies. We used a photomultiplier tube (H7422P-40, Hamamatsu) to detect the weak photons coming back from the retina. The output signals were amplified (HCA-1M-1M, Femto), low-pass-filtered (EF502, Thorlabs), and digitized (PCIE-1840, Advantech). To overcome the sensitivity limitation often observed in detecting fluorescence signals, we used our image registration software [27]. This approach uses the AO-OCT images to correct eye motion artifacts without requiring additional eye-tracking hardware, which enables tracking the subcellular features over time, regardless of the presence of fluorescence signals.

1.4 Subject interface:

We used a head and chin rest attached to a two-axis motorized stage (AU200-100X100-SC; OES Inc.) for the human subject interface. The stage, controlled by a joystick, enables a smooth translation of the head position parallel to the base floor with a sufficient travel distance to cover both eyes. In addition, the height was adjusted manually by a hand controller attached to the chin rest, like a standard clinical instrument. The subject sat and looked into a blue 2 mm diameter LED light displayed on the external fixation target (64x64 LED RGB Matrix Panel;

Adafruit). To image the targeted location, we controlled the position of the LED light (extended over $\sim 1.5^\circ$ in the retina) via Raspberry PI.

1.5. Workstation:

We used a research-grade workstation (SuperMicro SuperWorkstation 5049A-T) to handle multiple data acquisition boards, function generators, and a graphics card: (1) the spectrometers' camera acquisition boards (Xtium-CL MX4 with 80-bit mode Camera Link; Teledyne), (2) the SHWS's camera acquisition board (Emergent Vision), (3) a multifunction I/O device (NI PCI-6363e; NI), the DM's I/O interface (ALPAO), and (4) a GPU (NVIDIA Quadro RTX 4000). The operating system was Windows 10 Professional for Workstations (64-bit). To run several complicated tasks concurrently, we used a multi-core CPU (Intel Xeon Gold 6210U Processor 20-Core 2.5 GHz 27.5MB Cache; Intel) and a large enough memory (6 x 32GB PC4-23400 2933MHz DDR4 ECC RDIMM).

2. AO-OCT control software

The following section details the real-time control software running the AO-OCT system, which was split into two independent subsystems. We begin by describing the OCT subsystem and follow with a description of the AO subsystem – both of which made use of code contributed by Miller's lab at Indiana University School of Optometry. Instances where code was borrowed from Miller's team have been explicitly stated. Unless otherwise specified, all software was written by the Legacy Devers team.

2.1 System Control Software:

The OCT control software continuously acquires spectral interferograms at a speed of 250 kHz while driving the scanning mirrors (GM1 and GM2) to scan the sample tissue. At startup, the user specifies the number of A-scans per B-scan and B-scans per volume. Advanced options allow the user to swap the fast and slow scan axes, change the horizontal and vertical axes scan peak in degrees, and specify a horizontal and vertical offset in degrees. To sync the acquisition and the scanner movements, we used a multifunction I/O device (NI PCI-6363e; NI) to generate frame/line trigger signals and scanning waveforms. This signal generation section of code was contributed primarily from Miller's lab but was modified to work with our system's synchronization mechanisms. We used a modified raster scan that drives both fast/slow scanners with the triangular waveform to eliminate flyback, which can improve the image registration process, laser safety, and AO stability. Data is acquired using a signal generation thread and a separate thread managing synchronization and data acquisition. At the start of each volume pair, the sync/acquisition thread signals the generation thread to produce waveforms for one pair of volumes. The sync/acquisition thread then acquires one B-scan per B-scan period until each B-scan in the volume pair has been collected. This data is then processed with GPU/CPU in separate data processing threads and displayed to the user in the *en face* projection and cross-sectional views of the graphical user interface. Optionally, the user may choose to save a new video of data before its acquisition. In this case, the sync/acquisition thread proceeds as described but additionally sends a copy of the data to a separate saving thread, which writes the video data for each camera to binary files. The recorded data (raw spectra) were processed after each experiment (see Section 2.2.2). The control software was written in Visual Studio C++ using libraries such as CUDA, Qt5, Spera SDK, and NI-DAQmx.

The AO control software continuously acquires the SHWS camera images, computes the wavefront map, and controls the DM actuation in a feedback loop. At system start, the user specifies an approximate pupil size for the subject and optimizes it if needed. A precorrection is applied via the DM to cancel the large refractive errors (sphere and cylinder). During the operation, an acquisition thread runs continuously, monitoring each SHWS spot, identifying its local center of gravity (COG), and computing its sub-pixel displacement from the reference coordinate. The implementation of algorithms used in the COG and displacement computation

steps were written in C++ by Miller's lab. The SHWS spot displacements/slopes are converted and reported in the wavefront map, Zernike coefficients, and RMS wavefront error visualizations on the GUI. If the user activates the 'closed loop' process, an additional thread automatically adjusts the DM actuator voltages to correct aberrations using the formula $\mathbf{v}' = \mathbf{v} - g\mathbf{C}\mathbf{d}$, where \mathbf{v} is a vector of current actuator voltages, g is a constant gain value, \mathbf{C} is a control matrix, and \mathbf{d} is a vector of the new SHWS spot displacements (minus a target defocus vector that controls the focus position). The control matrix, mapping the SHWS spot displacements to the DM voltages, was prebuilt from poke matrices that were measured prior by poking each actuator sequentially. We generated several control matrices for different pupil sizes and numbers of SVD modes, allowing the user to select the control matrix specific to each subject. At this point, the voltage solution is corrected using a plane fitter class (originally written in Python by Miller's Lab at IUSO but rewritten in C++ by our team) to correct for tip and tilt in the DM. Typically, the SHWS was operated at 20 Hz with 49ms exposure during the operation. The computation time for the overall closed-loop operation was accelerated by multi-threaded computations for the COG measurements (3 lenslets at once; OpenMP). The software was primarily written in Visual Studio C++ using libraries including Qt5, ALPAO SDK, and Emergent Vision SDK. Freely available open-source software was also helpful in handling data operations, such as the Eigen and Open MP libraries for C++, in simplifying matrix calculations during closed-loop operations and the precorrection step.

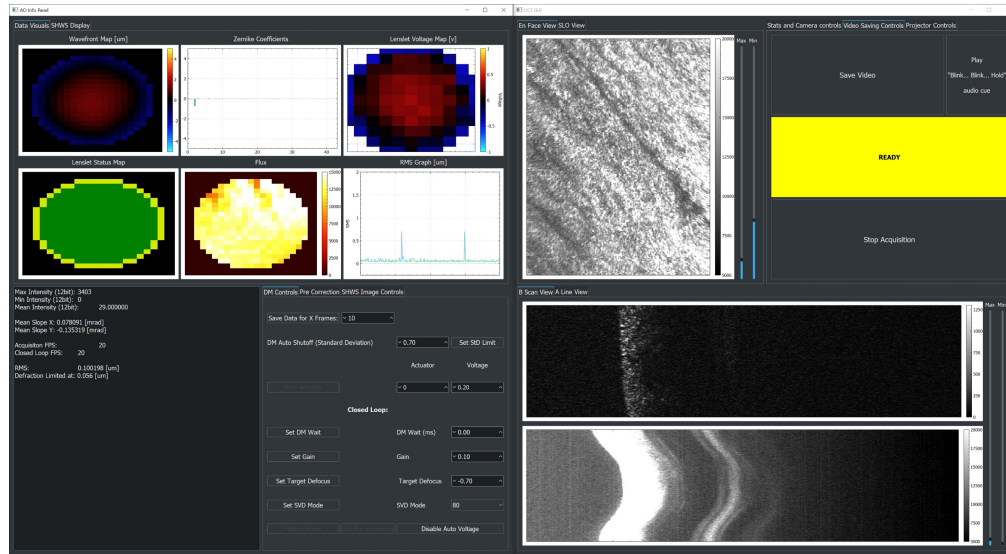


Fig. S2. The graphical user interfaces (GUIs) for (left) the AO subsystem and (right) the OCT subsystem. (left) The top section displays information about the status and aberration measured by the SHWS for each lenslet, as well as the actuator voltages applied to the DM. Below this, a window displays relevant statistics, and a panel holds operational controls. (right) The interface displays a live *en-face* projection, as well as a slow and fast B-scan (cross-sectional) views. In the upper right corner, controls for data acquisition are visible.

2.2 Graphical User Interface:

The AO system graphical user interface (GUI) in **Fig. S2 (left)** was designed to provide necessary information during data acquisition and allow for on-the-fly parameter tuning. The top section displays useful data visualizations, including a map of the measured wavefront, measured Zernike coefficients, an RMS wavefront error graph with a visual indicator for the value of diffraction-limited ($0.056 \mu\text{m}$), and a display of each DM actuator voltage. Displaying Zernike coefficients was helpful in determining a precorrection amount by which the 2nd-order Zernike coefficients (defocus and astigmatism) were minimized. The DM actuator map was

helpful in determining divergence, with the closed loop stopping automatically if the standard deviation of all actuator voltages goes above a user-controlled threshold - causing the voltages to return to the values created by the initial precorrection. The visualizations section includes a flux map and a lenslet status map, which reports whether each individual lenslet is reflecting enough light (green for bright spots, red for dim spots) or at the pupil's boundary (yellow) [28]. If a sufficient percentage of lenslets are in a dim state, the algorithm continues to store measurements from bright lenslets but does not update data visualizations until more lenslets are bright - preventing sudden changes when a subject blinks or moves out. Both the flux and lenslet status arrays are helpful in aligning the subject's eye with the scanning beam and determining blinking. Another tab allows the user to see the SHWS raw image in real time, with both reference and observed coordinates for each lenslet. This display is primarily used in calibrating the system before imaging subjects. Below, a statistics text window reports specific values including measured RMS error, acquisition frames per second, mean slope in milliradians, and mean light intensities. Next to this window is the control panel, which allows for beginning the closed loop, setting precorrection, and modifying values of gain, number of SVD modes, and target defocus, all changeable during the operation.

The main purpose of the OCT GUI in [Fig. S2 \(right\)](#) is to display to the user an en-face projection and real-time B-scan view. During acquisition, the top left corner holds a display for the en-face projection with display contrast sliders on the right side. These contrast sliders also adjust the display for the slow B-scan projection, which is located at the bottom of the screen and shows a B-scan averaged along the fast scan axis of the projection. Directly above the slow B-scan is the fast B-scan display, which shows the most recently acquired B-scan image. Used together, the two displays are useful for centering and correctly aligning layers of interest in a subject's eye. In the top right corner, a statistics window displays exact values for the measured intensities of both cameras. A panel also contains controls to switch all displays to show data from the bottom camera, top camera, or sum of both cameras. In another tab, a button allows for the user to start saving a video with a visual indicator to show the progress of the acquisition. An audio cue is played at the beginning and end of data collection, which is helpful for informing the subject when they may close or blink their eye.

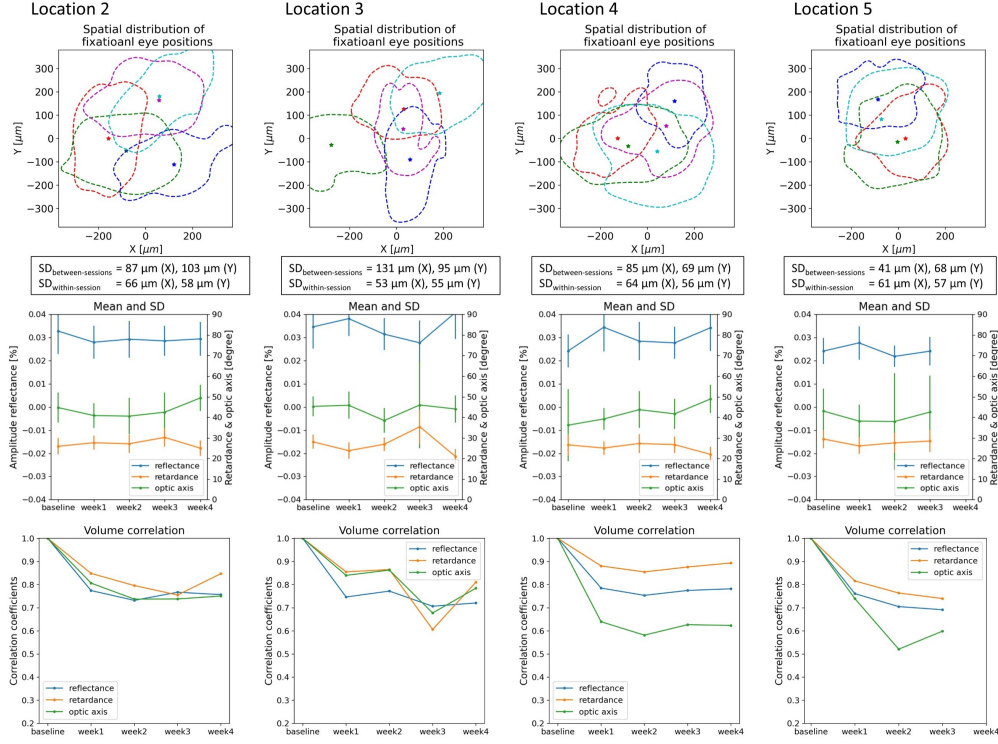


Fig. S3. Repeatability test results of peripapillary RNFL measurements at locations (2-5) in the right eye of a well-trained subject (H001). The first row is the spatial distribution of the eye positions tracked by our software at each location. The color-coded stars denote the mean positions of the eye motion trace. The color-coded isoline contours encompass 3SDs of the eye motion trace. The second row is the means and SDs of reflectance, retardance, and optic axis measured on the anterior surface of the RNFL within the overlap area. The third row is their volume correlation coefficients.

3. Assessing lateral resolution in AO-OCT image

To the best of our knowledge, there has been no standardized approach to evaluate the lateral resolution of AO-OCT. Such a practice is difficult for the following reasons: 1) OCT is a coherent imaging modality, limited by diffraction. 2) AO does not work well with a sample with a highly reflective smooth surface. Since the most commonly used resolution targets are highly reflective and directional, they do not capture real tissue imaging scenarios in which speckles are formed by backscattered light and obscuring low contrast features (e.g., GCL soma), in which AO corrects for wavefront aberrations by creating a pseudo-guide star with a scattering sample and allows for precise focus control. Thus, we chose to use a highly scattering heavy paper on which the test pattern was printed (RES-2; Newport) as a resolution test target so that both AO and OCT work together and better emulate a retinal imaging scenario. In addition, high contrast knife-edge-like printed patterns were used for assessing AO-OCT lateral resolution and contrast, since low contrast features are essentially invisible due to high-contrast frozen speckle patterns. To better describe these convoluted effects, we measured the resolution target with varying focus. **Figure S4** illustrates the impact of defocus on the test pattern visibility and the estimated $1/e^2$ beam waist spot radius. Image blur and reduced contrast are evident in their en face images (**Fig. S4 (a)**) and their line profiles (**Fig. S4 (b) left and center**; Group 4, Element 4) as we change target defocus with AO. Using Gaussian fit, we estimated the $1/e^2$ beam waist spot radius with varying defocus (**Fig. S4 (b) right**), showing a quadratic pattern consistent with image blur. However, the speckle size, estimated within the region

denoted by the red box using the complex-numbered autocorrelation method [29], shows no change with defocus. This confirms that high-contrast speckle patterns, whose size are insensitive to focus, obscure focus-sensitive low contrast features in AO-OCT images. In retinal imaging, averaging temporally varying speckles with precise focusing and alignment is, so far, the most successful approach to reduce speckle noise and appreciate AO-OCT image contrast and sharpness; however, this could not be replicated with a stationary sample because their speckles are frozen. Nonetheless, we were able to assess the lateral resolution of AO-OCT using this approach with high repeatability and reproducibility.

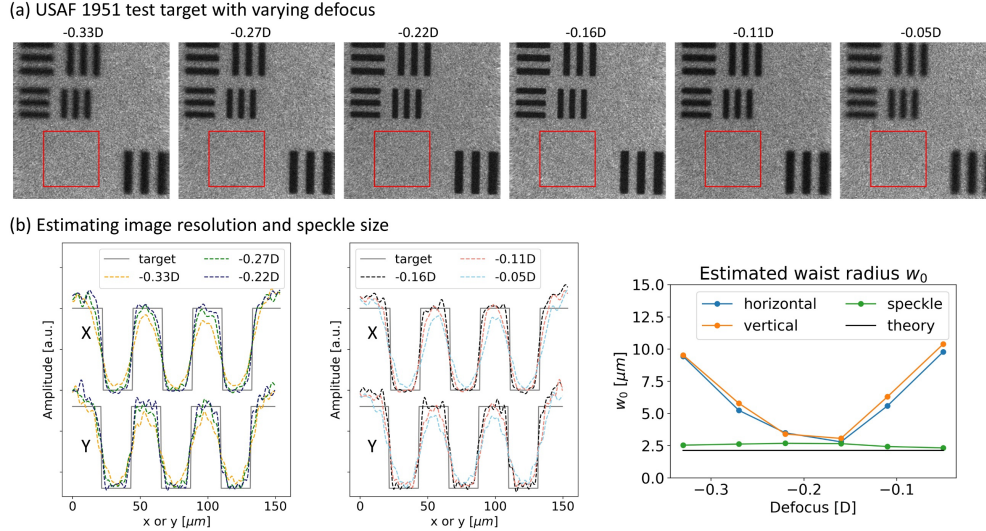


Fig. S4. Assessing AO-OCT lateral resolution using USAF 1951 test target (RES-2; Newport). (a) AO-OCT en-face image with varying focus. (b) Line profiles of Group 4, Element 4 (left and center). We estimated $1/e^2$ beam waist spot radius (right) with varying defocus. Speckle size was estimated at the region denoted by the red box using the method described in [29].

4. Myopia-related deformation within the temporal ONH

In the temporal ONH of H001, the reconstructed volumes show an extremely complicated view, convoluted with high myopia-related deformation (see [Fig. S4](#), [Visualization 4](#), and [Visualization 5](#)). The laminar beams appeared narrowed and stretched near the transition zone from the prelaminar to the laminar regions (at Z0, Z1, and Z2), as indicated by the yellow arrowheads, compared to those in the posterior laminar region (at Z4) and central ONH (see [Fig. 8](#) and [Visualization 2](#)). The laminar insertion, where the anterior laminar beams directly connected to the scleral tissue, was found just below the Bruch's membrane opening denoted by the red arrowhead in [Fig. 8](#) (see also [Visualizations 4 and 5](#)). No apparent border tissue nor choroidal tissue was visible between the two in this subject H001. The axon bundle (or dark trunk-like structure) passed through the LC via a deformed path as indicated by the green arrows. The retardance image shows its moderate increase in the laminar region and its significantly greater increase in the scleral region (aka exposed scleral flange [30]), which could indicate the change in the collagenous fiber density, distribution, and arrangement, as in part similar to the central ONH. However, unlike central ONH, the retardance was elevated in the nerve fiber region, as it came closer to the disc margin, as a consequence of the axon bundles bending away from the imaging beam axis. Therefore, the moderate color difference in the optic axis image at Z0 represents the nerve fiber orientation, whereas the dramatic alteration of the optic axis in the laminar and scleral regions (Z3 and Z4) indicates the change in their collagenous fiber orientation. As a recent study shows evidence for a close relationship between myopia-related collagenous remodeling and increased scleral birefringence [31], it would be of

great interest to test its association with stretched laminar beam and axon bundle birefringence that are now individually resolved by AO-OCT polarimetry.

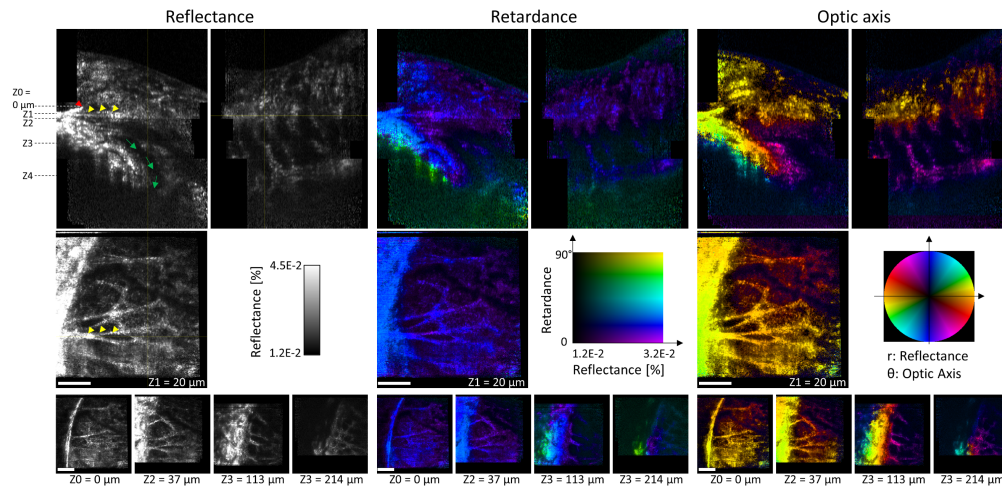


Fig. S5. Revealing the temporal ONH microarchitecture in a 37-year-old subject with high myopia (-7D). AO-OCT reflectance (left), retardance (center), and optic axis orientation (right) are shown. The color change in the retardance and optic axis images represents their value change, which follows their respective color maps. The red arrowhead indicates the Bruch's membrane opening. The yellow arrowheads indicate the laminar beam insertion. The green arrowheads indicate the path of the axon bundle (or dark trunk-like structure).

References

1. S. Jiao, W. Yu, G. Stoica, and Lihong V. Wang, "Optical-fiber-based Mueller optical coherence tomography," *Opt. Lett.* **28**, 1206–1208 (2003).
2. B. H. Park, M. C. Pierce, and J. F. de Boer, "Comment on "Optical-fiber-based Mueller optical coherence tomography,"" *Opt. Lett.*, *OL* **29**, 2873–2874 (2004).
3. W. Träsichker, S. Zotter, T. Torzicky, B. Baumann, R. Haindl, M. Pircher, and C. K. Hitzenberger, "Single input state polarization sensitive swept source optical coherence tomography based on an all single mode fiber interferometer," *Biomed. Opt. Express* **5**, 2798–2809 (2014).
4. N. Lippok, M. Villiger, C. Jun, and B. E. Bouma, "Single input state, single-mode fiber-based polarization-sensitive optical frequency domain imaging by eigenpolarization referencing," *Opt. Lett.*, *OL* **40**, 2025–2028 (2015).
5. M. R. Hee, D. Huang, E. A. Swanson, and J. G. Fujimoto, "Polarization-sensitive low-coherence reflectometer for birefringence characterization and ranging," *J. Opt. Soc. Am. B* **9**, 903–908 (1992).
6. K. Schoenenberger, B. W. Colston, D. J. Maitland, L. B. Da Silva, and M. J. Everett, "Mapping of Birefringence and Thermal Damage in Tissue by use of Polarization-Sensitive Optical Coherence Tomography," *Appl. Opt.* **37**, 6026–6036 (1998).
7. C. Hitzenberger, E. Goetzinger, M. Sticker, M. Pircher, and A. Fercher, "Measurement and imaging of birefringence and optic axis orientation by phase resolved polarization sensitive optical coherence tomography," *Opt. Express* **9**, 780–790 (2001).
8. M. Mujat, B. H. Park, B. Cense, T. C. Chen, and J. F. de Boer, "Autocalibration of spectral-domain optical coherence tomography spectrometers for in vivo quantitative retinal nerve fiber layer birefringence determination," *J. Biomed. Opt.* **12**, 041205–041205 (2007).
9. G. Häusler and M. W. Lindner, "'Coherence Radar" and "Spectral Radar"—New Tools for Dermatological Diagnosis," *Journal of Biomedical Optics* **3**, 21–31 (1998).
10. M. Pircher, E. Götzinger, B. Baumann, and C. K. Hitzenberger, "Corneal birefringence compensation for polarization sensitive optical coherence tomography of the human retina," *JBO* **12**, 041210 (2007).
11. C. Fan and G. Yao, "Mapping local retardance in birefringent samples using polarization sensitive optical coherence tomography," *Opt. Lett.*, *OL* **37**, 1415–1417 (2012).
12. J. Porter, H. Queener, J. Lin, K. Thorn, and A. A. S. Awwal, *Adaptive Optics for Vision Science: Principles, Practices, Design and Applications*, 1st ed. (Wiley-Interscience, 2006).
13. K. M. Hampson, R. Turcotte, D. T. Miller, K. Kurokawa, J. R. Males, N. Ji, and M. J. Booth, "Adaptive optics for high-resolution imaging," *Nat Rev Methods Primers* **1**, 1–26 (2021).

14. R. H. Webb, G. W. Hughes, and F. C. Delori, "Confocal scanning laser ophthalmoscope," *Appl. Opt.* **26**, 1492–1499 (1987).
15. S. A. Burns, R. Tumber, A. E. Elsner, D. Ferguson, and D. X. Hammer, "Large-field-of-view, modular, stabilized, adaptive-optics-based scanning laser ophthalmoscope," *J. Opt. Soc. Am. A* **24**, 1313–1326 (2007).
16. A. Gómez-Vieyra, A. Dubra, D. Malacara-Hernández, and D. R. Williams, "First-order design of off-axis reflective ophthalmic adaptive optics systems using afocal telescopes," *Opt. Express* **17**, 18906–18919 (2009).
17. K. Kurokawa, D. Tamada, S. Makita, and Y. Yasuno, "Adaptive optics retinal scanner for one-micrometer light source," *Opt. Express* **18**, 1406–1418 (2010).
18. J. J. Hunter, B. Masella, A. Dubra, R. Sharma, L. Yin, W. H. Merigan, G. Palczewska, K. Palczewski, and D. R. Williams, "Images of photoreceptors in living primate eyes using adaptive optics two-photon ophthalmoscopy," *Biomed. Opt. Express*, BOE **2**, 139–148 (2011).
19. W. S. T. Lam and R. Chipman, "Balancing polarization aberrations in crossed fold mirrors," *Appl. Opt.*, AO **54**, 3236–3245 (2015).
20. J. M. Bueno and J. Jaronski, "Spatially resolved polarization properties for in vitro corneas," *Ophthalmic and Physiological Optics* **21**, 384–392 (2001).
21. B. Cense, W. Gao, J. M. Brown, S. M. Jones, R. S. Jonnal, M. Mujat, B. H. Park, J. F. de Boer, and D. T. Miller, "Retinal imaging with polarization-sensitive optical coherence tomography and adaptive optics," *Opt. Express* **17**, 21634–21651 (2009).
22. M. J. Ju, Y.-J. Hong, S. Makita, Y. Lim, K. Kurokawa, L. Duan, M. Miura, S. Tang, and Y. Yasuno, "Advanced multi-contrast Jones matrix optical coherence tomography for Doppler and polarization sensitive imaging," *Opt. Express* **21**, 19412–19436 (2013).
23. Y. Geng, A. Dubra, L. Yin, W. H. Merigan, R. Sharma, R. T. Libby, and D. R. Williams, "Adaptive optics retinal imaging in the living mouse eye," *Biomed. Opt. Express* **3**, 715–734 (2012).
24. R. Maddipati and P. Tankam, "Development of high-speed, integrated high-resolution optical coherence microscopy and dual-channel fluorescence microscopy for the simultaneous co-registration of reflectance and fluorescence signals," *Optics and Lasers in Engineering* **149**, 106823 (2022).
25. O. Packer, L. C. Diller, J. Verweij, B. B. Lee, J. Pokorny, D. R. Williams, D. M. Dacey, and D. H. Brainard, "Characterization and use of a digital light projector for vision research," *Vision Research* **41**, 427–439 (2001).
26. K. Franke, A. Maia Chagas, Z. Zhao, M. J. Zimmermann, P. Bartel, Y. Qiu, K. P. Szatko, T. Baden, and T. Euler, "An arbitrary-spectrum spatial visual stimulator for vision research," *eLife* **8**, e48779 (2019).
27. K. Kurokawa, J. A. Crowell, N. Do, J. J. Lee, and D. T. Miller, "Multi-reference global registration of individual A-lines in adaptive optics optical coherence tomography retinal images," *JBO* **26**, 016001 (2021).
28. A. de Castro, L. Sawides, X. Qi, and S. A. Burns, "Adaptive optics retinal imaging with automatic detection of the pupil and its boundary in real time using Shack-Hartmann images," *Appl. Opt.*, AO **56**, 6748–6754 (2017).
29. K. Kurokawa, S. Makita, Y.-J. Hong, and Y. Yasuno, "In-plane and out-of-plane tissue micro-displacement measurement by correlation coefficients of optical coherence tomography," *Optics Letters* **40**, 2153 (2015).
30. S. Hong, H. Yang, S. K. Gardiner, H. Luo, G. P. Sharpe, J. Caprioli, S. Demirel, C. A. Girkin, C. Y. Mardin, H. A. Quigley, A. F. Scheuerle, B. Fortune, A. Jiravarnsirikul, C. Zangalli, B. C. Chauhan, and C. F. Burgoyne, "OCT Optic Nerve Head Morphology in Myopia III: The Exposed Neural Canal Region in Healthy Eyes – Implications for High Myopia," *American Journal of Ophthalmology* **0**, (2023).
31. X. Liu, L. Jiang, M. Ke, I. A. Sigal, J. Chua, Q. V. Hoang, A. W. Chia, R. P. Najjar, B. Tan, J. Cheong, V. Bellemo, R. S. Chong, M. J. A. Girard, M. Ang, M. Liu, G. Garhöfer, V. A. Barathi, S.-M. Saw, M. Villiger, and L. Schmetterer, "Posterior scleral birefringence measured by triple-input polarization-sensitive imaging as a biomarker of myopia progression," *Nat. Biomed. Eng* 1–15 (2023).